# Mapping of Thermal Indices Using an Automated Landsat 8-based-ArcGIS Model: A Case Study in Alexandria City, Egypt

**Sharaf El Din, E.,[1*] Elsherif, A.,[1] Ramadan, S.[1] and Aboelkhair, H.[2]**
[1]Tanta University, Faculty of Engineering, Public Works Engineering Department, Tanta, Gharbeya, Egypt
E-mail: essam.helmy@f-eng.tanta.edu.eg*
[2]Tanta University, Faculty of Arts, Department of Geography and Geographical Information Systems, Tanta, Gharbeya, Egypt
*Corresponding Author*

**DOI: https://doi.org/10.52939/ijg.v19i9.2823**

**Abstract**
*Urbanization is a contributing factor to global warming, as asphalt, concrete, and other light-absorbing materials replace vegetated areas, causing an increase in Land Surface Temperature (LST) and creating Surface Urban Heat Islands (SUHI). Although thermal satellite imagery has been a powerful tool in mapping LST and SUHI spatio-temporal changes, the number of studies in Africa, including Egypt, remains limited. Thus, in this research, an automated model was developed in ArcGIS and used to map LST and SUHI and detect Urban Hot Spots (UHS) in Alexandria city, Egypt, using Landsat 8 time series (2013 to 2021). The results revealed an increase of 38.35% in urban areas and a decrease of 50.79% in agricultural areas, a change that was demonstrated by a decline in the Normalized Difference Vegetation Index (NDVI) from 0.84 in 2013 to 0.53 in 2021. Correspondingly, LST and SUHI displayed an increasing pattern, with the highest recorded values observed in 2021. Thus, this study showed the negative impact of urbanization on Alexandria city's temperature – a city that is already facing a climate catastrophe because of the sea level rise resulting from climate change. Furthermore, the developed estimation model can be similarly useful for climate change researchers and decision makers.*

**Keywords:** Climate Change, Global Warming, Landsat 8, Land Surface Temperature Surface Urban Heat Island

## 1. Introduction

Temperature is globally increasing because of climate change [1]. Urbanization is one of the main factors that negatively impacts climate. It is a complex activity that involves the conversion of natural land cover into man-made features, including urban and industrial areas, in order to generate various spatial outlines, which are formed and controlled by aspects linked to the transportation network and physical features [2] and [3]. In the past few decades, the observed growth of built environment has not been concentrated around the major cities, but around small and rural zones [4].

Urbanization has produced a noticeable decline in rural and vegetated zones by transforming natural green areas into artificial surfaces, such as concrete, asphalt, and metal. These non-evaporating surfaces have different thermal conductivities, which negatively influence Land Surface Temperature (LST) and regional climate [5]. In addition, green/vegetated regions transport cooling effects to both air and LST [6]. The cooling benefits generated by vegetation, which occur mainly because of evapotranspiration, altitude, and shading, consume solar energy [6] [7] [8] and [9]. Therefore, the main cause of urban/non-urban temperature variance is linked to alterations in thermal characteristics of the glowing surfaces and declined rates of evapotranspiration in built-up regions [10]. Surface urban heat island (SUHI) is formed due to the expansion of metropolitan regions and can be defined as the process in which temperature is higher in built-up environments than adjacent non-urban regions [11].


ISSN: 1686-6576 (Printed) | ISSN 2673-0014 (Online) | 

The negative effects of SUHI include a rise in thermal discomfort, a growth in energy consumption, a sharp rise in air pollution, a noticeable reduction in water quality, and a raise in per capita water consumption, especially in summer.

Several studies of monitoring the impact of urbanization on climate and meteorology have been implemented around the globe using in-situ data [12] and [13]. In-situ measurements can be used to obtain accurate regional temperatures; however, these strategies are labour intensive, time and effort consuming, and cost-prohibitive, especially on a large scale [11] and [14]. Thus, remote sensing offers major benefits over conventional methods, mainly because of the temporal reliability and synoptic coverage [15] and [16]. Hence, remote sensing is an applicable tool to estimate LST in both spatial and temporal domains by means of satellite devices, which provide thermal infrared data [11]. Moreover, remote sensing has the potential to achieve SUHI and to understand its direct influences on the environment. The derived LST is the main key for SUHI calculations, and consequently a primary step for categorizing urban hot spots (UHS). In this context, previous research studies have used the normalized difference vegetation index (NDVI) as an effective proxy to study the effects of LST and SUHI on urban zones [17] [18] [19] and [20]. Additionally, landscape constructions are linked to LST that is influenced by both land use and land cover (LULC) categories [21].

Considering the time interval of 1985–2020, approximately 93% of previous studies related to LST and SUHI estimation have focused on regions in Asia, North America, and Europe. Conversely, only 2% of the research studies included areas in Africa [21]. Thus, this study aims to develop a novel Landsat 8-based-ArcGIS model to estimate LST and SUHI from thermal data and investigate their spatio-temporal variations in the city of Alexandria, Egypt. To the best of our knowledge, this study is the first to build an automated model to map LST, SUHI, and UHS on Alexandria, Egypt. Alexandria, a Mediterranean coastal city, was chosen as a study site because: 1) it is Egypt's second largest city after Cairo, and its busiest port, 2) It is a UNESCO heritage site of a great archeological and historical importance, and 3) it is one of the Mediterranean cities that are at a grave risk of getting partially or fully submerged under the Mediterranean Sea in the future as a result of sea level continuous rise, formed by global warming.

To reach the goal of this study, an automated model was developed in ArcGIS and used to achieve the following objectives: (1) to map LULC variations in the study site; (2) to compute NDVI, emissivity, and LST per pixel using the developed ArcGIS model; (3) to determine LST and NDVI association; (4) to map both LST and SUHI spatio-temporal distribution; and (5) to detect UHS. Mapping LST and SUHI and detecting UHS can help in further quantifying and understanding how global warming impacts Alexandria's climate, which will help decision makers to come up with site-specific mitigation programs. Furthermore, the developed estimation model, being semi-automated and user friendly, can be a powerful asset in future studies associated to the influences of climate change on LST and SUHI, both in Alexandria city and globally.

## 2. Material and Methods

The upcoming sections describe the study site, the utilized Landsat 8 data, and details of the method used in the retrieval of NDVI, LST, SUHI, and UHS from the satellite imagery. The developed method was implemented in an automated ArcGIS model.

### *2.1 Study Area*

Alexandria extends along the Mediterranean coast about 114 miles (183km) northwest of Cairo, Egypt [22]. The latitude and longitude coordinates of Alexandria are: 31.205753 N, 29.924526 E, as shown in Figure 1. The city covers 300 square kilometres and has a Mediterranean climate. Winter appears stormy and rainy. It has an average temperature of 37°C in August, while the average is 18°C in January. Alexandria has a population of 5.5 million and it is considered as the largest seaport in Egypt. It serves more than 50% of all of the country's imports and exports [22]. The 2015 and 2020 floods had catastrophic social and economic impacts on the city. Three-meter-high waves, twice the maximum wave height previously recorded in the city, flooded the Corniche, Alexandria's major coastal traffic corridor, turning it into part of the Mediterranean. The waves slammed into buildings, forcing many families to flee their homes, and killing at least six people. In December 2021, the city saw snow for the first time in decades, which resulted in ports closures and school suspension. As stated by The United Nations (UN) Intergovernmental Panel on Climate Change (IPCC), Alexandria is facing a climate catastrophe as the Mediterranean Sea level continues to rise because of global warming, threatening to send one third of the city underwater by 2050. This means that approximately 25 to 30% of the city's population will be forced to flee their homes as the flooded regions become uninhabitable [22].

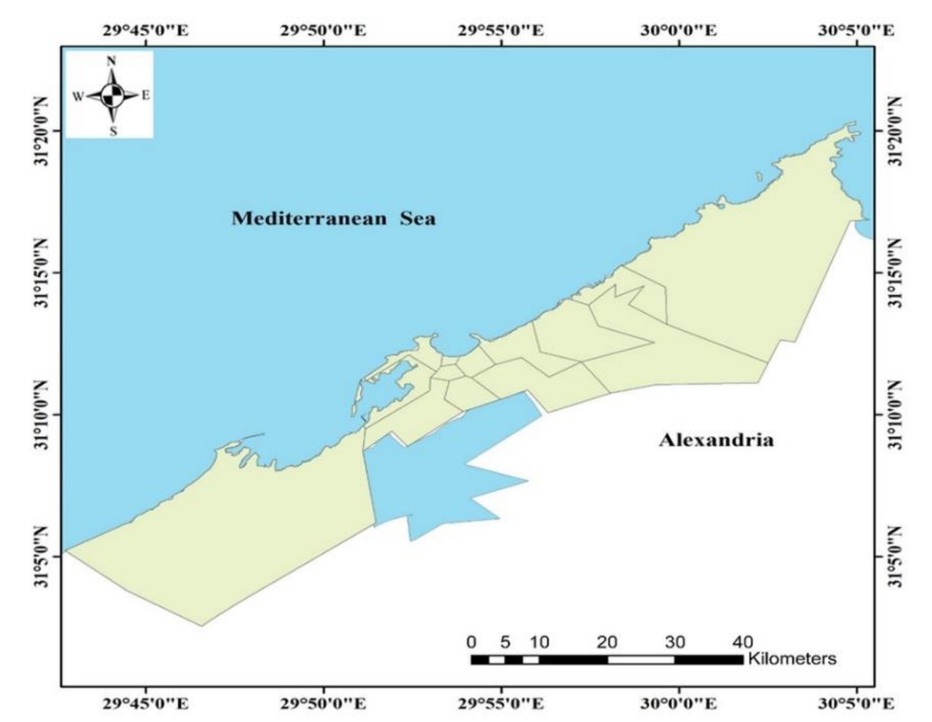


**Figure 1**: The study site of Alexandria, Egypt

*2.2 Satellite Data*

The Landsat 8 satellite, developed by NASA and the United States Geological Survey (USGS), was launched in 2013 as a continuation of the Landsat program. The Landsat 8 payload involves two sensors: the Operational Land Imager (OLI) and the Thermal Infrared Sensor (TIRS). OLI and TIRS offer spatio-temporal scenes at 15 meters (panchromatic), 30 meters (multispectral), and 100 meters (thermal), resampled to 30 meters [23]. Level 1T Landsat 8 data are accessible at no cost. Level 1T scenes supports effective geometric accuracy by integrating ground control points (GCPs) and a Digital Elevation Model (DEM) for topographic accuracy. Nominated GCPs were employed to rectify Landsat 8 scenes to the Universal Transverse Mercator (UTM) projection, World Geodetic System 1984 (WGS 84) [23].

Landsat 8 satellite scenes utilized in this study were downloaded from the USGS, as shown in Figure 2. Only satellite imagery with less than 10% cloud coverage were carefully taken from 2013 to 2021. A total of nine images were used in the analyses. The utilized Landsat 8 scenes were captured on 27 April 2013, 16 May 2014, 7 August 2015, 12 October 2016, 26 May 2017, 14 July 2018, 15 June 2019, 5 September 2020, and 6 July 2021. The images were gathered at various months/years to best distinguish the maximum alteration in LST. The reflective bands from Landsat 8 were used to map NDVI, LST, SUHI, and UHS.

*2.3 Land Use and Land Cover Classification (LULC)*

To study spatio-temporal variations in the patterns of LULC in the study site between 2013 and 2021, supervised classification was carried out using the satellite scenes acquired on 27 April 2013 and 6 July 2021. The dominant purpose of image classification was the formation of thematic maps of various land cover. Maximum likelihood method was applied to categorize the images into different classes with similar characteristics. For this, training samples were chosen from Landsat 8 images and accuracy assessment (i.e., the error matrix) was utilized to evaluate the performance of maximum likelihood method to LULC classification by comparing the classified data with ground truth data (i.e., Google Earth images), which were acquired around the same time of Landsat 8 satellite images.

Based on the classification process, pixels were grouped into five primary LULC: urban, rural, agriculture, water, and bare earth. The urban class stands for industrial and residential sections, such as cities, industries, new/old buildings, and concrete. The rural class involves villages and small settlements. The agricultural class includes vegetated districts, reclaimed lands, and harvested zones. The water class acts for water bodies, such as sea water and drainage canals.


ISSN: 1686-6576 (Printed) | ISSN 2673-0014 (Online) | © Geoinformatics International


**Figure 2**: Landsat 8 satellite subscene used in our study

Finally, bare earth class includes bare surfaces where natural vegetation is absent or almost absent. Post-classification was employed for computing different types of change among the obtained thematic maps. In this context, change detection was applied to detect variations in the LULC classes, and these alterations can describe the influence of anthropogenic activities, including urbanization and other behaviours on the environment.

*2.4 Landsat 8 Processing Steps and Land Surface Temperature (LST) Estimation*

LST values were calculated using the developed Landsat 8-based-ArcGIS- model, as simplified in Figure 3. The automated model showed a friendly user interface, which allows the user to input the raw data (i.e., Landsat 8 data) and the output (i.e., spatial distribution maps for Landsat 8 thermal indices, such as LST) can be simply obtained. First, Landsat 8 digital numbers are saved in 16 bits unsigned integer format. Equation 1 was employed to rescale digital numbers ($Q_{cal}$) to obtain at-sensor spectral radiance ($L_\lambda$) using the radiometric rescaling coefficients ($M_L$ and $A_L$) and the correction factor ($O_i$) of the Landsat 8 multispectral data [23].

$$L_\lambda = M_L Q_{cal} + A_L - O_i$$

Equation 1

At-sensor spectral radiance ($L_\lambda$) was transformed into brightness temperature ($BT$) using Band-specific thermal conversion constants ($K_1$ and $K_2$) from Landsat 8 metadata, as shown Equation 2 [23].

$$B_T = \left[ \frac{K_2}{Ln\left(\frac{K_1}{L_\lambda}\right) + 1} \right] - 273.15$$

Equation 2

After that, to obtain the results of brightness temperature ($BT$) in Celsius, radiant temperature was adjusted by adding -273.15°C, as shown in Equation 2. Equation 3 was then employed to compute $NDVI$. The calculations of $NDVI$ was essential because, subsequently, the proportion of vegetation ($P_V$), which was extremely related to $NDVI$, and emissivity ($\varepsilon$), which was associated to the $P_V$, must be calculated.

$$NDVI = \frac{Band5 - Band4}{Band5 + Band4}$$

Equation 3

Both minimum and maximum values of $NDVI$ were utilized to calculate $P_V$, as indicated in Equation 4:

$$P_V = \left[ \frac{NDVI - NDVI_{\min}}{NDVI_{\max} - NDVI_{\min}} \right]^2$$

Equation 4

Emissivity ($\varepsilon$) was simply calculated as a function of $NDVI$ and $P_V$ using Equation 5:

$$\varepsilon = 0.004 P_V + 0.986$$

Equation 5

After words, the land surface temperature (LST) was obtained from LST equation as shown in Equation 6:


ISSN: 1686-6576 (Printed) | ISSN 2673-0014 (Online) | © Geoinformatics International

$$LST = \frac{BT}{1+\left(\frac{0.0010895BT}{1.4388}\right)Ln(\varepsilon)}$$

Equation 6

*2.5 Calculations of Surface Urban Heat Island (SUHI) Indices*

The variation in *LST* between urban environment ($LST_{urban}$) and surrounding regions or rural area ($LST_{rural}$), agriculture ($LST_{agriculture}$), and ($LST_{water}$) represents SUHI intensity [24].

SUHI intensity values were measured from the following rules as specified in Equations 7 to 9:

$$SUHI_1 = LST_{urban} - LST_{rural}$$

Equation 7

$$SUHI_2 = LST_{urban} - LST_{agriculture}$$

Equation 8

$$SUHI_3 = LST_{urban} - LST_{water}$$

Equation 9

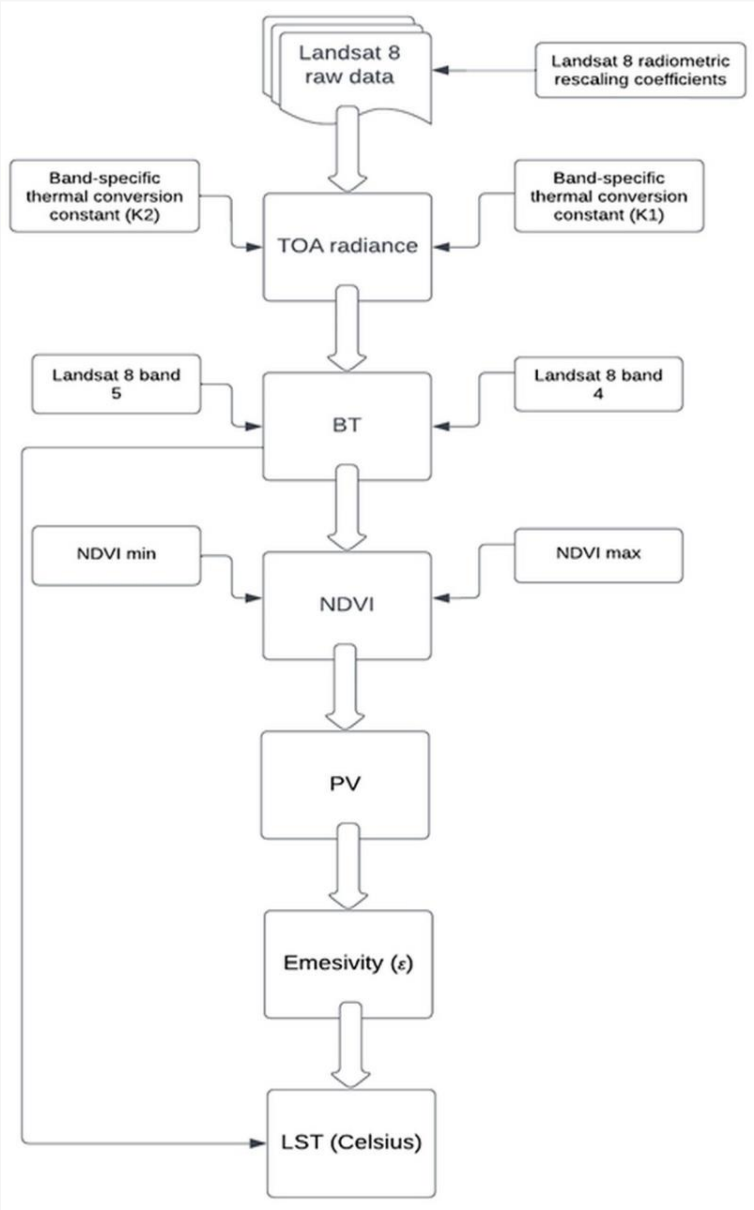


**Figure 3**: Study workflow

*2.6 Classification of Urban Hot Spots (UHS)*

LST spatial distribution maps were managed to classify *UHS* (the most warmed/heated zones in an urban region) [25]. As indicated in Equation 10, *UHS* can be considered for pixels, which have:

$$LST \geq \mu + 2\sigma$$

Equation 10

where $\mu$ is the mean *LST* of the urban spot, and $\sigma$ is the standard deviation.

## 3. Results and Discussion

The present study attempts to measure LST from Landsat 8 spectral information. This work is additionally extended to map spatio-temporal transformations of SUHI, and to categorize UHS.

*3.1 LULC Spatio-Temporal Variation*

Through the maximum likelihood classification method, LULC maps were produced using the following dates: (27 April 2013 (the earliest date) and 6 July 2021 (the latest date)), as clarified in Figure 4. A Kappa coefficient of 0.90 and an overall accuracy of 92.31% was achieved for the earliest scene; while, for the latest scene, the Kappa coefficient was 0.91 and the overall accuracy was 93.44%. A LULC difference/change map for the 2013-2021 period was produced, highlighting the regions in which the LULC modified in the study area during the nominated interval. The total area and proportion of each LULC class was demonstrated in Table 1.

The results revealed that both urban and agriculture were the LULC classes with the most significant changes, as stated in Table 1. Due to urban sprawl in the specified period, the regions related to the urban class increased from 26.18% to 36.22%. On the other hand, the area linked to the agriculture class declined from 25.00% to 12.34%. It was noticed that the study area was subjected to continuous spatio-temporal changes through the entire interval of study (2013–2021). Anthropogenic activities, urban expansion, land reclamation, and urban development are the major aspects inducing the LULC classes in the selected study site. Some zones are representative cases of the impact of developmental projects, specifically urbanization, on LULC. These zones are connected to urban growth with a noticeable increase of 38.35%. This was synchronized with a remarkable decrease in agricultural zones of 50.79%. Moreover, rural areas and water bodies increased by 21.27% and 12.24%, respectively. Additionally, bare earth class was found to be declined by 28.66% in 2021, and this rise was exploited to increase both rural and built-up regions.

*3.2 NDVI and LST Spatio-Temporal change*

The NDVI spatio-temporal distribution maps demonstrated a distinct phase in which the highest values of NDVI covering larger areas were detected between spring and summer months, meaning that throughout the spring season the vegetation biomass achieve their maximum. Conversely, the lowest NDVI values were observed in autumn and winter months, as shown in Figure 5. Moreover, there was an obvious decrease of agricultural zones over the years as the mean value of NDVI declined from 0.84 in 2013 to 0.53 in 2021 due to urban growth and development. The unique LST samples are linked to the thermal properties of land cover sets. In order to recognize the influence of LULC classes on LST, thermal characteristics of each land cover class were considered, and consequently spatio-temporal changes of LST in the study site were illuminated in Figure 6.

In all utilized satellite imageries, the LST were higher in urban regions compared to other classes, but during the summer season, the gradient from urban and rural areas turned higher. The LST maps demonstrated high temperatures in urban spots due to the impact of surface materials, such as buildings, asphalt, concrete, and parking lots. In other words, the transformation of natural surfaces onto artificial environment is the main cause of LST increase in the study region.

**Table 1**: The sum of area and total percentage of change for each class in the change map

| **Class** | **Sum of area ($m^2$) 2013** | **Total area (%) 2013** | **Sum of area ($m^2$) 2021** | **Total area (%) 2021** | **Total area of change (%)** |
|---|---|---|---|---|---|
| Urban | 844,409,706.1 | 26.18 | 1,164,399,682 | 36.22 | + 38.35 |
| Rural | 157,817,148 | 4.89 | 190,692,351.9 | 5.93 | + 21.27 |
| Agriculture | 806,250,876.8 | 25.00 | 396,747,107.2 | 12.34 | - 50.79 |
| Water | 1,117,525,841 | 34.65 | 1,250,188,656 | 38.89 | + 12.24 |
| Bare Earth | 299,407,603.3 | 9.28 | 212,824,477.4 | 6.62 | - 28.66 |


ISSN: 1686-6576 (Printed) | ISSN  2673-0014 (Online) | © Geoinformatics International

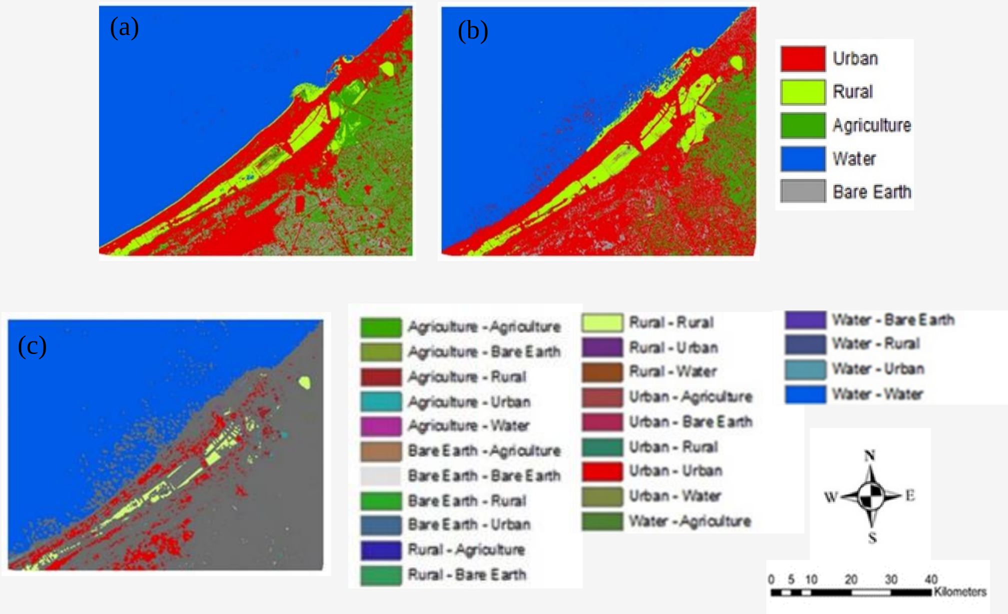


**Figure 4**: LULC maps of the selected study area referent to (a) 27 April 2013, (b) 6 July 2021, and (c) LULC change from 27 April 2013 to 6 July 2021

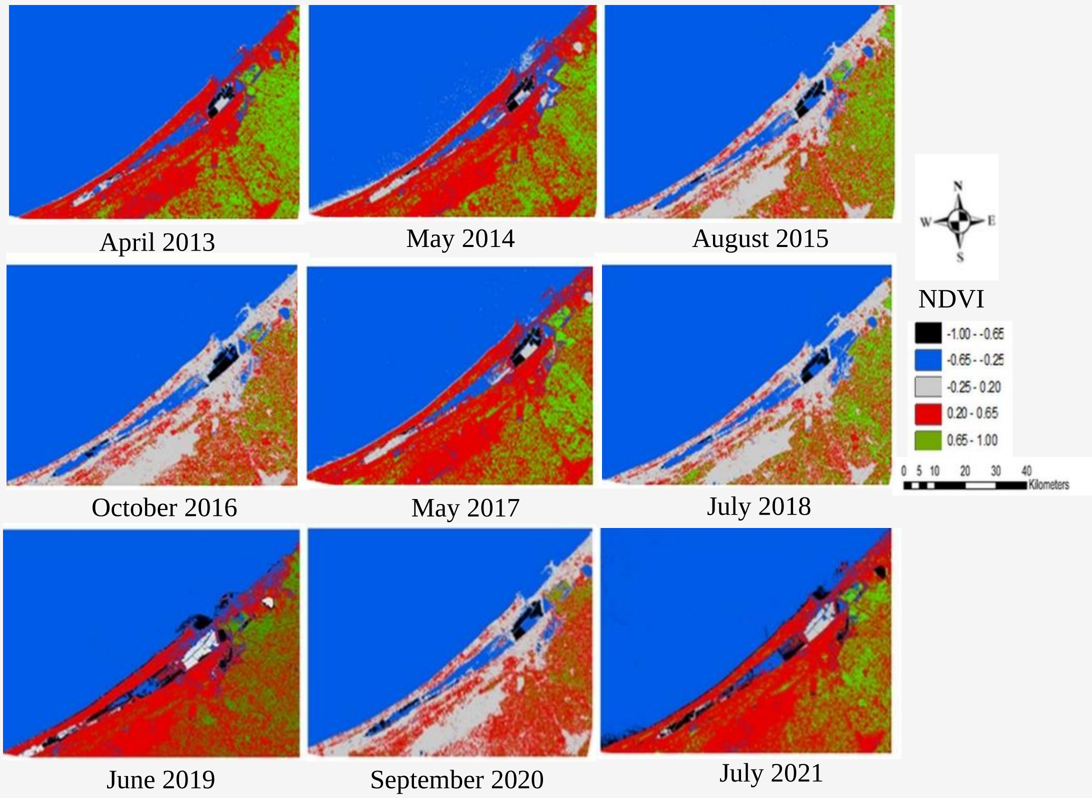


**Figure 5**: Spatio-temporal distribution of NDVI from 2013 to 2021


ISSN: 1686-6576 (Printed) | ISSN 2673-0014 (Online) | © Geoinformatics International

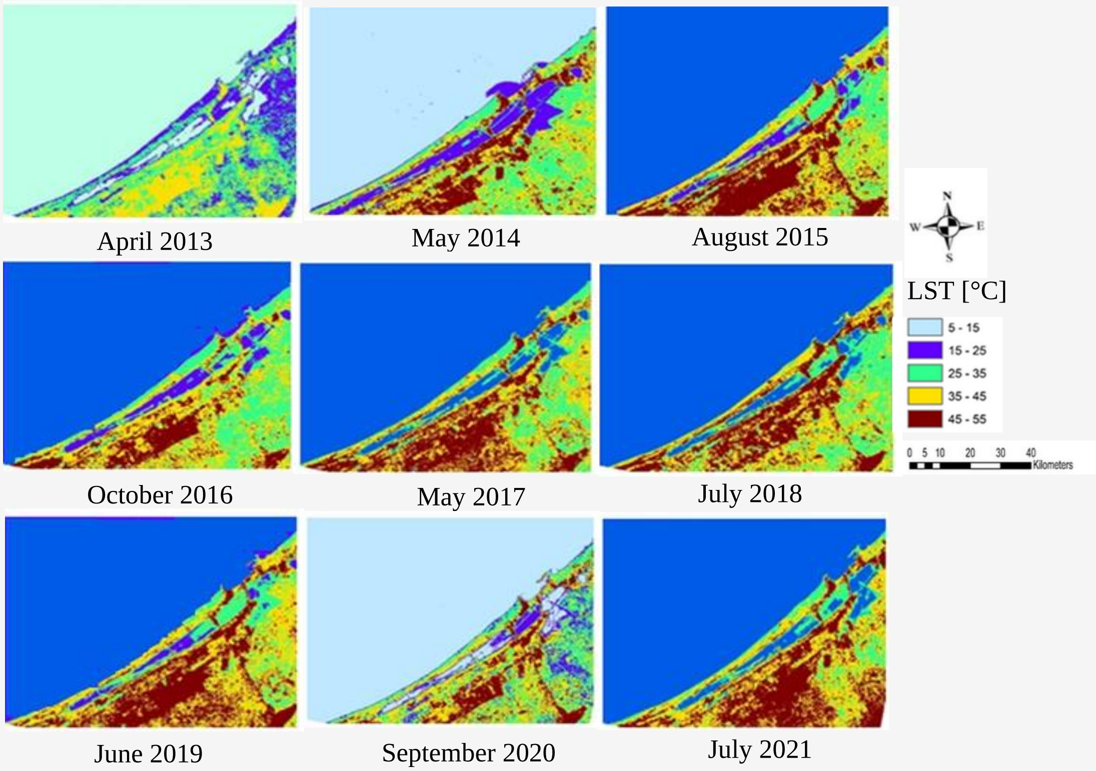


**Figure 6**: Spatio-temporal change of LST in Celsius from 2013 to 2021

During the Summer season, the months of August 2015, May 2017, July 2018, June 2019, and July 2021 demonstrated the highest temperatures for urban zones followed by the months of April 2013, October 2016, and September 2020. The coolest month between the acquired dates was observed in October 2016 (i.e., during Autumn). Moreover, rural zones were found to be hotter throughout summer; however, the temperature of rural areas was lower than the values in urban zones. In all acquired scenes, lower temperatures were detected in water and agricultural areas, which helps to minimize the temperature of the surfaces throughout the direct influence of evapotranspiration and shading.

The surface temperature change can be detected in all months owing to the surface coverage. In this context, the lowest temperature happened in October (i.e., Autumn of 2016) and followed by April 2013. In contrast, the highest temperature occurred in July (i.e., Summer of 2021) and followed by June 2019, as shown in the obtained LST spatial distribution maps (Figure 7). Mean LST of each LULC class in the study site can be arranged in a descending order as follows; urban, bare earth, rural, agriculture, and water bodies. A noticeable increase in LST quantities of each LULC class was monitored and reached the highest records in 2021. Continuous rise in LST from 2013 to 2021 was attributed to the enhanced industrialization and urbanization rates in the study area at this specific period. This is because the study area was mainly covered by green areas in 2013, which can reflect less energy leading to acceptable LST levels. On the other hand, in 2021, the selected study area was full of anthropogenic activities and man-made features that can show more energy and high levels of LST. As a result, the continuous increase in LST can reflect a natural warming trend of the climate.

### *3.3 Estimation of Surface Urban Heat Island (SUHI) Indices*

For each LULC class, mean LST was calculated for each Landsat 8 image acquisition date (i.e., from 2013 to 2021), as shown in Table 2. Throughout the whole period of the research study, the maximum and minimum LST estimates were detected in urban and water regions, respectively. The LST difference among LULC classes was very high in summer, but very low in autumn. Additionally, high-rise built-up zones blocked the blowing of the breeze, preserving hot air in the downtown regions. Therefore, computing SUHI intensity during the whole period (2013 to 2021) is essential.

**Table 2**: Mean LST values in Celsius for the selected LULC classes from 2013 to 2021

| Date/class | Urban | Rural | Agriculture | Water | Bare Earth |
|---|---|---|---|---|---|
| April 2013 | 35.90 | 23.50 | 18.70 | 12.10 | 27.50 |
| May 2014 | 44.80 | 24.60 | 19.20 | 12.70 | 30.90 |
| August 2015 | 46.10 | 26.20 | 22.30 | 18.50 | 33.80 |
| October 2016 | 32.70 | 22.20 | 18.20 | 11.90 | 26.10 |
| May 2017 | 47.30 | 29.10 | 21.40 | 16.10 | 37.80 |
| July 2018 | 51.00 | 32.70 | 26.50 | 21.10 | 41.20 |
| June 2019 | 52.20 | 33.10 | 27.20 | 21.50 | 42.00 |
| September 2020 | 36.10 | 26.60 | 22.50 | 16.70 | 29.50 |
| July 2021 | 54.30 | 33.90 | 27.80 | 22.60 | 43.10 |

**Table 3**: SUHI intensity values in Celsius (urban-rural, urban-agriculture, and urban-water)

| Acquisition date | $SUHI_1$ | $SUHI_2$ | $SUHI_3$ |
|---|---|---|---|
| April 2013 | + 12.40 | + 17.20 | + 23.80 |
| May 2014 | + 20.20 | + 25.60 | + 32.10 |
| August 2015 | + 19.90 | + 23.80 | + 27.60 |
| October 2016 | + 10.50 | + 14.50 | + 20.80 |
| May 2017 | + 18.20 | + 25.90 | + 31.20 |
| July 2018 | + 18.30 | + 24.50 | + 29.90 |
| June 2019 | + 19.10 | + 25.00 | + 30.70 |
| September 2020 | + 9.50 | + 13.60 | + 19.40 |
| July 2021 | + 20.40 | + 26.50 | + 31.70 |

The SUHI intensity values were calculated in Celsius, as shown in Table 3. In this context, the average urban-rural LST differences were obtained, and the maximum values were observed in summer, while the minimum values were detected during autumn. Moreover, the urban-agriculture index yielded high intensity values in late spring and early summer. Because of LST alterations between agricultural spaces and built-up zones in day and night, results of the urban-agriculture index showed extreme seasonal changes (i.e., maximum values were obtained in summer (July 2021), and minimum values were observed in autumn (September 2020)). Furthermore, the third SUHI index (urban-water) revealed that the maximum SUHI intensity values were observed in summer due to the extreme temperature variance between urban regions and water areas. The maximum SUHI intensity values with all three indices (SUHI1, SUHI2, and SUHI3) were + 20.40, + 26.50, and + 32.10 Celsius, respectively.

The influence of high temperatures obviously originated from urban/industrial regions, where a group of high-rise buildings and industries are located. On the other hand, The minimum SUHI intensity values with all three indices (SUHI1, SUHI2, and SUHI3) were + 9.50, + 13.60, and + 19.40 Celsius, respectively. Furthermore, the third SUHI index (urban-water) revealed that the maximum SUHI intensity values were observed in summer due to the extreme temperature variance between urban regions and water areas. The maximum SUHI intensity values with all three indices (SUHI1, SUHI2, and SUHI3) were + 20.40, + 26.50, and + 32.10 Celsius, respectively. The influence of high temperatures obviously originated from urban/industrial regions, where a group of high-rise buildings and industries are located. On the other hand, The minimum SUHI intensity values with all three indices (SUHI1, SUHI2, and SUHI3) were + 9.50, + 13.60, and + 19.40 Celsius, respectively.

### *3.4 Classification of Urban Hot Spots (UHS)*

By using SUHI indices, it is possible to categorize UHS. The results indicated that the most heated sites were found in urbanized/industrial zones of the study site, coinciding with the locations, which have the maximum SUHI intensity values. UHS were concentrated in urban zones, which are distinguished by the absence of green spaces, shadowed areas, and water bodies. Among the whole locations presented in the study site, built-up areas, industrial zones, large parking lots, asphalt, concrete blocks, and shopping centers were classified as UHS, as shown in Figure 7.


ISSN: 1686-6576 (Printed) | ISSN  2673-0014 (Online) | © Geoinformatics International

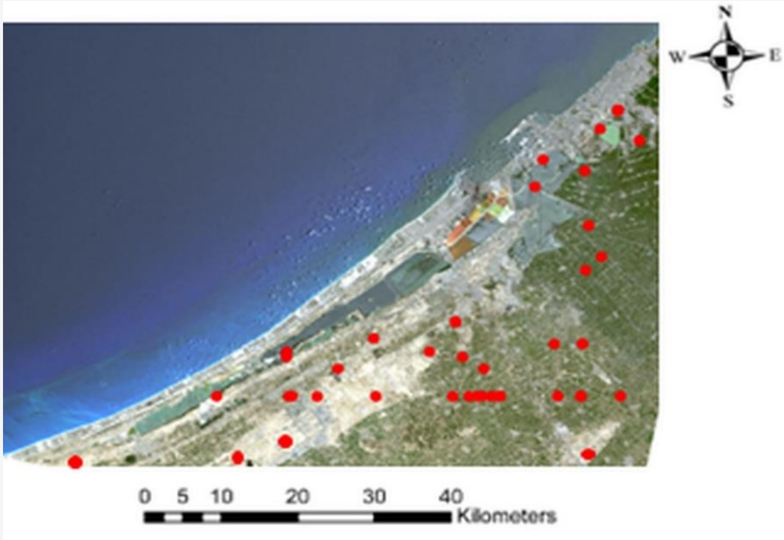


**Figure 7**: UHS (in red dots) spatial distribution map for the selected study site

Urban areas tend to be warmer than their surroundings because of various causes, such as low albedo, type of materials used in the construction process, lack of vegetation, and heat preservation. Additionally, most of the identified UHS are locations of superior anthropogenic activities, with extensive heat generation and emissions, which are considered as significant factors to heat increase and global temperature rise. These anthropogenic activities also involve land use transformation from agricultural to urban, as well as burning up agricultural wastes, specifically the rice straws after the harvest season during summer.

## 4. Conclusion

The Egyptian authority makes significant attempts to manage the continuous increase in LST due to the unplanned urban expansion/development on expense of green/agricultural fertile lands. Consequently, this research project has been initiated to develop Landsat 8-based-ArcGIS model to monitor and assess spatio-temporal variations in LULC, and consequently to study their negative impacts on both LST and the environment. The current research study uses the district scale to identify the annual changes in LULC in Alexandria Governorate, Egypt based on nine Landsat 8 satellite scenes (2013 to 2021).

Results indicated that most of the agricultural regions in the selected study area were transformed into urban areas as a result of urban sprawl, where urban locations increased by 41.31% in 2021. In contrast, agricultural regions declined by 49.51% from 2013 to 2021. Moreover, spatio-temporal mapping of LST confirmed that UHS belong to urbanized/industrial and built-up regions within the city boundary, coinciding with the regions that have the highest SUHI values. Hence, classifying UHS is crucial for environmental monitoring and sustainable development. Additionally, SUHI indices illustrated that the best thermal comfort was linked to the existence of vegetation. It can be noted that the integration of remote sensing and geographic information systems can be employed to investigate spatio-temporal variations in LULC classes and LST, and to assess the negative influence of anthropogenic activities on the environment. Finally, to achieve the maximum advantage from this research study, results should be discussed with decision makers to take the right action at the proper time in order to save the environment. Regardless of the remarkable observations brought by the results, some limitations should be considered in future work, such as specific spectral indices of built-up materials, as well as correlation between LST and other factors, such as air temperature and surface features, and finally how to mitigate temperatures in UHS.

**Acknowledgements**

This research work is supported by the Egyptian Ministry of Higher Education, represented by Public Works Engineering Department, Faculty of Engineering, Tanta University. The author wishes to acknowledge the USGS Landsat Archive Center for the Landsat 8 Level 1T imagery.

## References


[1] Antrop, M., (2000). Changing Patterns in the Urbanized Countryside of Western Europe. *Landscape Ecology*, Vol. 15(3), 257-270. https://doi.org/10.1023/A:1008151109252.

[2] Pickett, S. T., Cadenasso, M. L., Grove, J. M., Boone, C. G., Groffman, P. M., Irwin, E., Kaushal, S. S., Marshall, V., McGrath, B. P., Nilon, C. H., Pouyat, R. V., Szlavecz, K., Troy, A. and Warren, P., (2011). Urban Ecological Systems: Scientific Foundations and a Decade of Progress. *Journal of Environmental Management*, Vol. 92(3), 331–362. https://doi. org/10.1016/j.jenvman.2010.08.022.

[3] Forman, R. T. T., (2014). *Urban Ecology: Science of Cities*. Cambridge. Cambridge University Press.

[4] Andrade-Nunez, M. J. and Aide, T. M., (2018). Built-up Expansion between 2001 and 2011 in South America Continues Well Beyond the Cities. *Environmental Research Letters*, Vol. 13, 256-263. https://doi.org/10.1088/1748-9326 /aad2e3.

[5] Shiflett, S. A., Liang, L. L., Crum, S. M., Feyisa, G. L., Wang, J. and Jenerette, G. D., (2017). Variation in the Urban Vegetation, Surface Temperature, Air Temperature Nexus. *The Science of the Total Environment*, Vol. 579, 495–505. https://doi.org/10.1016/j.scitotenv.20 16.11.069.

[6] Taha, H., Akbari, H., Rosenfeld, A. and Huang, J., (1988). Residential Cooling Loads and the Urban Heat Island-The Effects of Albedo. *Building and Environment*, Vol. 23(4), 271–283. https://doi.org/10.1016/0360-1323(88)900 33-9.

[7] Grimmond, C. S. B. and Oke, T. R., (1991). An Evapotranspiration-Interception Model for Urban Areas. *Water Resources Research*, Vol. 27(7), 1739–1755. https://doi.org/10.1029/91 WR00557.

[8] Imhoff, M. L., Zhang, P., Wolfe, R. E. and Bounoua, L., (2010). Remote Sensing of the Urban Heat Island Effect Across Biomes in the Continental USA. *Remote Sensing of Environment*, Vol. 114(3), 504–513. https://doi. org/10.1016/j.rse.2009.10.008.

[9] Jenerette, G. D., Harlan, S. L., Buyantuev, A., Stefanov, W. L., Declet-Barreto, J., Ruddell, B. L., Myint, S. W., Kaplan, S. and Li, X., (2016). Micro-Scale Urban Surface Temperatures are Related to Land-Cover Features and Residential Heat Related Health Impacts in Phoenix, AZ USA. *Landscape Ecology*, Vol. 31(4), 745–760. https://doi.org/10.1007/s10980-015-0284-3.

[10] Streutker, D. R., (2002). A Remote Sensing Study of the Urban Heat Island of Houston, Texas. *International Journal of Remote Sensing*, Vol. 23(13), 2595–608. https://doi.org/ 10.1080/01431160110115023.

[11] Zhou, D., Xiao, J., Bonafoni, S., Berger, C., Deilami, K., Zhou, Y., Frolking, S., Yao, R., Qiao, Z. and Sobrino, J. A., (2019). Satellite Remote Sensing of Surface Urban Heat Islands: Progress, Challenges, and Perspectives. *Remote Sensing*, Vol. 11(1). https://doi.org/10.3390/ rs11010048.

[12] Tao, W., Liu, J., Ban-Weiss, G. A., Hauglustaine, D., Zhang, L. Z., Zhang, Q., Cheng, Yu, Y. and Tao, S., (2015). Effects of Urban Land Expansion on the Regional Meteorology and Air Quality of Eastern China. *Atmospheric Chemistry and Physics*, Vol. 15, 8597–8614. https://doi.org/10.5194/acp-15-859 7-2015.

[13] Hu, X. M., Xue, M. and Klein, P. M., (2016). Analysis of Urban Effects in Oklahoma City Using a Dense Surface Observing Network. *Journal of Applied Meteorology and Climatology*, Vol. 55(3), 723–741. https://doi. org/10.1175/JAMC-D-15-0206.1.

[14] Owen, T. W., Carlson, T. N. and Gillies, R. R., (1998). An Assessment of Satellite Remotely Sensed Land Cover Parameters in Quantitatively Describing the Climatic Effect of Urbanization. *International Journal of Remote Sensing*, Vol. 19, 1663–1681. https://doi.org/ 10.1080/014311698215171.

[15] Sharaf El Din, E. and Zhang, Y., (2017). Neural Network Modelling of the Saint John River Sediments and Dissolved Oxygen Content from Landsat OLI Imagery. *The International Archives of the Photogrammetry, Remote Sensing and Spatial Information Sciences*. 245-249. https://doi.org/10.5194/isprs-archives-XLI I-4-W4-245-2017.

[16] Sharaf El Din, E., (2019). Enhancing the Accuracy of Retrieving Quantities of Turbidity and Total Suspended Solids using Landsat-8-Based-Principal Component Analysis Technique. *Journal of Spatial Science*, Vol. 66(3), 493-512. https://doi.org/10.1080/14498 596.2019.1674197.

[17] Pettorelli, N., Vik, J. O., Mysterud, A., Gaillard, J. M., Tucker, C. J. and Stenseth, N. C., (2005). Using the Satellite-Derived NDVI

to Assess Ecological Responses to Environmental Change. *Trends in Ecology & Evolution,* Vol. 20(9), 503–510. https://doi.org/10.1016/j.tree. 2005.05.011.

[18] Hou, G., Zhang, H. and Wang, Y., (2011). Vegetation Dynamics and its Relationship with Climatic Factors in the Changbai Mountain Natural Reserve. *Journal of Mountain Science*, Vol. 8(6), 865–875. https://doi.org/10.1007/s11 6 29-011-2206-4.

[19] Yang, H., Yang, X., Heskel, M., Sun, S. and Tang, J., (2017). Seasonal Variations of Leaf and Canopy Properties Tracked by Ground-Based NDVI Imagery in a Temperate Forest. *Scientific Reports*, Vol. 7(1). https://doi.org/ 10.1038/s41598-017-01260-y.

[20] Rani, M., Kumar, P., Pandey, P. C. Srivastava, P. K., Chaudhary, B. S., Tomar, V. and Mandal, V. P., (2018). Multi-temporal NDVI and Surface Temperature Analysis for Urban Heat Island Inbuilt Surrounding of Sub-Humid Region: A Case Study of Two Geographical Regions. *Remote Sensing Applications: Society and Environment*, Vol. 10, 163–172. https://doi. org/10.1016/j.rsase.2018.03.007.

[21] Zhou, W., Qian, Y., Li, X., Li, W. and Han, L., (2014). Relationships Between Land Cover and the Surface Urban Heat Island: Seasonal Variability and Effects of Spatial and Thematic Resolution of Land Cover Data on Predicting Land Surface Temperatures. *Landscape Ecology*, Vol. 29, 153–167. https://doi.org/ 10.1007/s10980-013-9950-5.

[22] Al-Arabiya News, (2021). Retrieved July 7, 2022, from https://english.alarabiya.net/ views/ news/middle-east/2021/09/01/Alexandri a-will-sink-beneath-the-water-if-Egyptians-don-t-hel p-fight-climate-change.

[23] United States Geological Survey (USGS). (2021). Retrieved May 10, 2022, from http://landsat.usgs.gov/Landsat8_Using_Produ ct.php.

[24] Huang, Q., Huang, J., Yang, X., Fang, C. and Liang, Y., (2019). Quantifying the Seasonal Contribution of Coupling Urban Land Use Types on Urban Heat Island using Land Contribution Index: A Case Study in Wuhan, China. *Sustainable Cities and Society*, Vol. 44, 666–675. https://doi.org/10.1016/j.scs.2018.10.016.

[25] Guha, S., Govil, H. and Mukherjee, S., (2017). Dynamic Analysis and Ecological Evaluation of Urban Heat Islands in Raipur City, India. *Journal of Applied Remote Sensing*, Vol. 11(3). https://doi.org/10.1117/1.JRS.11.036020.